

Temperature and potential dependence electrochemical impedance studies of LiMn_2O_4

Surender Kumar · Prasant Kumar Nayak ·
Krishnan S. Hariharan · N. Munichandraiah

Received: 3 June 2013 / Accepted: 3 August 2013 / Published online: 13 August 2013
© Springer Science+Business Media Dordrecht 2013

Abstract Detailed analysis of alternating current impedance data of LiMn_2O_4 electrodes measured at several temperatures and potentials was carried out. The Nyquist plots generally consisted of semicircles corresponding to two time constants. However, at low temperatures (-10 to 10°C) and potential region between 3.90 and 4.20 V , three time constants were present. The third semicircle present at the middle to high frequency range was attributed to electronic resistance of LiMn_2O_4 . Impedance parameters were evaluated using appropriate electrical equivalent circuits. From the temperature dependence of resistive parameters, activation energy values for the corresponding processes were calculated.

Keywords Lithium-ion battery · Cathode material · Impedance · Electronic resistance · Activation energy

1 Introduction

Lithium-ion batteries have gained increasing importance in multi-utility applications, which include small scale energy utilities such as portable electronic and optical devices at

present as well as large scale utilities such as electric vehicles and load-levelling of electric grids in future [1–3]. Among the several positive electrode materials studied for Li-ion battery application, the use of manganese-based oxides has stimulated interest due to their low cost, safety and environmental compatibility [4, 5]. The spinel LiMn_2O_4 was proposed by Thackeray et al. [4] and it was extensively developed for commercial application [6–8]. The structure of spinel LiMn_2O_4 with space group $Fd\bar{3}m$ is described as layers of close packed oxygen atoms, in which Li and Mn ions occupy tetrahedral and octahedral sites, respectively. In the framework, MnO_6 octahedra share edges to build a rigid three dimensional network with open interconnected channels in (110) direction where Li^+ ions are accommodated. Li^+ -ions are mobile facilitating their reversible extraction and insertion.

Electrochemical impedance spectroscopy (EIS) is a versatile experimental technique for non-destructive characterization of electrochemical cells [9]. The technique involves the measurement of response of electrochemical cell to a small alternating current (ac) signal over a wide frequency range. The analysis of EIS data allows separation of resistive and capacitive components (some times, inductive components as well) and, therefore, several electrochemical parameters can be evaluated [10]. The ac impedance measurements of several battery systems were reported and reviewed [11–15]. Studies on the effect of state-of-charge (SOC) and temperature of commercial Li-ion cells were reported by our group [16, 17]. The data were analysed using an equivalent circuit and non-linear least squares (NLLS) fitting procedure, and impedance parameters of commercial Li-ion cells were evaluated. The resistance corresponding to the electron-transfer reactions exhibited a strong dependence on SOC and also on

S. Kumar · P. K. Nayak · N. Munichandraiah (✉)
Department of Inorganic and Physical Chemistry, Indian
Institute of Science, Bangalore 560012, India
e-mail: muni@ipc.iisc.ernet.in

K. S. Hariharan
India Science Lab, General Motors Global R&D,
Bangalore 560066, India

Present Address:
K. S. Hariharan
Samsung Advanced Institute of Technology India, SISO Pvt.
Ltd., Bangalore 560093, India

temperature [16, 17]. The measurements of impedance of Li-ion cells have been employed to study the effect of additives to the electrolytes [18–21], the performance of various electrode materials [22–26], etc., in addition to characterization of commercial Li-ion cells [16, 17, 27–30]. Application of electrical equivalent circuit models on the basis of impedance properties is an appropriate procedure for modelling of Li-ion batteries for prediction of their performance [27]. Among the various forms of representation of EIS data, Nyquist plot is a convenient representation, which generally consists of one or more semicircles, each semicircle representing a parallel combination of a resistance and a capacitance [10, 31].

Recently, EIS of the spinel LiMn_2O_4 was studied for Li^+ ion insertion and de-insertion at different potentials and different temperatures by Zhuang et al. [32]. At intermediate degrees of intercalation, three semicircles appeared in the Nyquist impedance diagram against two semicircles generally observed. At temperature $>20^\circ\text{C}$, the high frequency semicircle and the middle to high frequency semicircle overlapped. The effects of electronic and ionic transport properties of LiMn_2O_4 were separated in EIS spectra recorded at low temperatures. An equivalent circuit model taking account of this rare observation was proposed [32].

In the present study, temperature and potential dependence studies of LiMn_2O_4 positive electrode material are investigated in detail by EIS. Appearance of three semicircles in the Nyquist diagram is reproducible similar to the results of Zhuang et al. [32]. The analysis of impedance data is carried out using appropriate equivalent circuits. The impedance parameters thus obtained are analyzed for their dependences on potential and temperature. The variations of resistances with temperature are analysed by Arrhenius-like relationships and apparent activation energies of the corresponding transport properties are evaluated. To the best of authors' knowledge, this type of analysis is not reported for LiMn_2O_4 electrodes in the literature.

2 Experimental

Spinel LiMn_2O_4 , lithium ribbon (0.3 mm thick), ethylene carbonate (EC), dimethyl carbonate (DMC), LiPF_6 , poly(vinylidene fluoride) (PVDF) and *n*-methyl pyrrolidone (NMP) were purchased from Aldrich. Powder X-ray diffraction (XRD) pattern and scanning electron microscopy studies of LiMn_2O_4 suggest that crystal structure corresponds to the spinel form (JCPDS File no. 35-782) and the particles are distributed over a broad range of size (Fig. 1a, b). For electrochemical studies, LiMn_2O_4 electrodes were fabricated on stainless steel (SS) disks as the

current collectors. Before fabrication, a commercial grade SS foil disk (diameter 16 mm) was dipped in 30 % dilute HNO_3 for about 5 min, washed with running water, rinsed with doubly distilled water followed by acetone and dried in air. LiMn_2O_4 (80 wt%), acetylene carbon black (Alfa Aesar) (15 wt%) and PVDF (5 wt%) were mixed, ground in a mortar, and a few drops of NMP were added to get an ink. The ink was applied on the pre-treated SS disk of area 2.0 cm^2 and dried at 110°C for about 30 min. The coating and drying steps were repeated to achieve a loading level of 5.0 mg cm^{-2} . Finally, the electrodes were dried at 110°C under vacuum for 12 h. A Mettler Toledo electronic balance model AB265-S/FACT with 0.01 mg sensitivity was used for weighing the electrodes. Coin-type cells (CR 2025) were assembled using a Li foil for the counter electrode in coin cell containers purchased from Hohsen Corporation, Japan. Prior to the cell assembly, the surface of Li ribbon was scraped to remove surface film. A micro-porous polypropylene film (Celgard model 2400) was used as the separator and the electrolyte was 1 M LiPF_6 in 1:1 (v/v) mixed solvents of EC and DMC. The mixed solvent was repeatedly percolated through a column of molecular sieves to remove any traces of moisture before the preparation of the electrolyte. Preparation of the mixed solvent, its purification, electrolyte preparation and cell assembly were carried out in an Ar atmosphere glove box (MBraun model UNILAB).

Galvanostatic charge–discharge cycling was performed by Bitrode battery cycle-life tester. Impedance spectra were recorded at various potentials with an ac excitation signal of 5 mV over the frequency range from 100 kHz to 0.01 Hz using Solartron frequency response analyzer model 1255B and Solartron electrochemical interface model 1287. Impedance data were subjected to NLLS fitting procedure using ZView software supplied by Solartron. The temperature controlled experiments were performed in the range from -10 to 50°C by using a Julabo refrigerator-cum heater Model F25, with ethylene glycol–water mixture (1:1 v/v) as the thermal medium. For this purpose, the coin cell was mounted inside a Teflon sealed glass container with an outer jacket and the thermal medium was circulated through the outer jacket. The cell temperature was measured with an accuracy of $\pm 0.1^\circ\text{C}$ by a thermocouple placed adjacent to the cell.

The impedance studies were carried out at thirteen different temperatures starting from -10 to 50°C in the voltage range of 3.50–4.30 V after completing two charge–discharge cycles. At first, the electrode was charged to the required value of voltage at room temperature ($22\text{--}24^\circ\text{C}$) and then the temperature was reduced to -10°C and equilibrated for 30 min before recording impedance spectrum. Then the temperature was increased by 5°C and the experiment was repeated. This procedure was repeated for

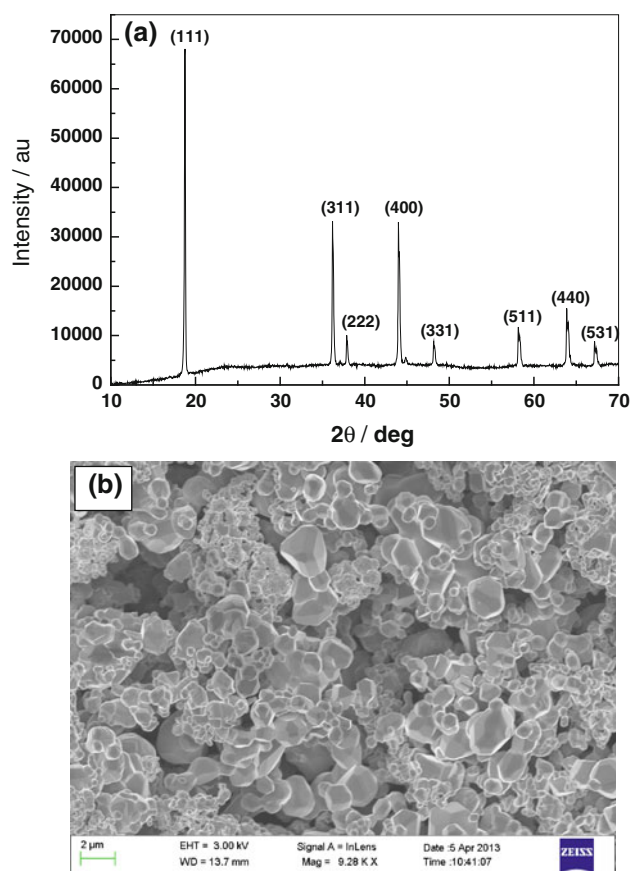
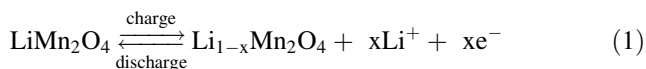


Fig. 1 **a** Powder XRD pattern and **b** SEM image of LiMn_2O_4

all temperatures. Once the experiments were completed at a given potential, the cell was allowed to reach the ambient temperature, it was charged to the next higher potential and impedance spectra were recorded at different temperatures similar to the experiments carried out at the previous potential.

3 Results and discussion

A $\text{Li-LiMn}_2\text{O}_4$ coin cell was subjected to charge–discharge cycling at C/5 rate, and the variation of cell voltage with time is shown in Fig. 2a. The differential capacity plot is shown in Fig. 2b. There are two voltage plateaus observed in Fig. 2a during both charge and discharge processes (Reaction 1), which are clearly noticed in Fig. 2b as peaks.



The first discharge plateau appears at 4.10 V and the second plateau peak at 3.98 V (Fig. 2b). The corresponding charging plateaus appear at 4.02 and 4.14 V, respectively. Cyclic voltammetric current peaks of LiMn_2O_4 electrode reported in the literature appear at potentials

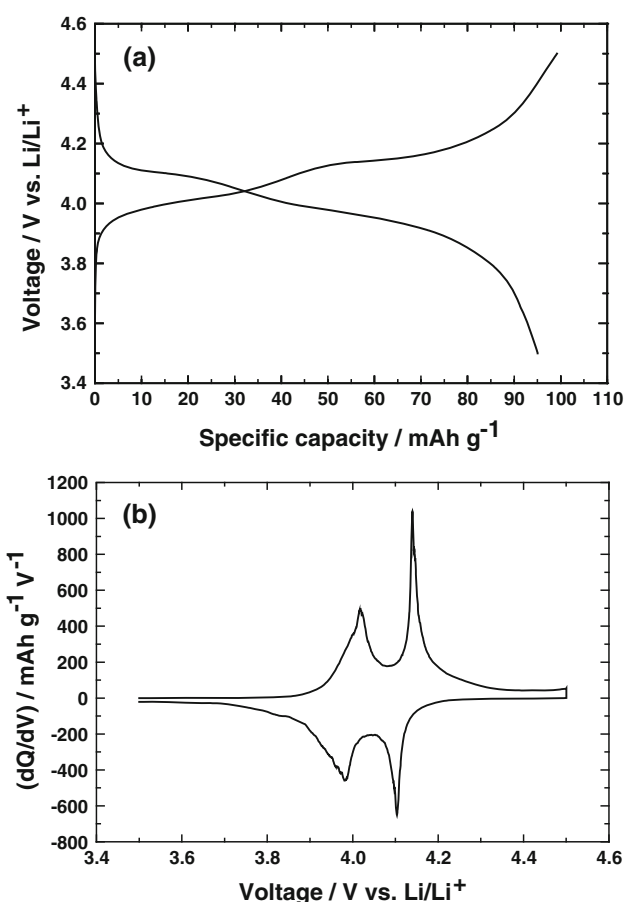


Fig. 2 **a** Charge–discharge curves of $\text{Li/LiMn}_2\text{O}_4$ cell at C/5 rate and **b** derivative plot of charge–discharge curve. Area: 2.0 cm^2 and mass of LiMn_2O_4 : 5.0 mg cm^{-2}

corresponding to the peaks present in Fig. 2b [33, 34]. The first plateau corresponds to intercalation/de-intercalation of Li^+ in the range $1 \leq x \leq 0.5$ in $\text{Li}_x\text{Mn}_2\text{O}_4$ into/from the half of the tetrahedral sites where Li–Li interactions are present. The second potential plateau is due to the same process occurring in the range $0.5 \leq x \leq 0$ in $\text{Li}_x\text{Mn}_2\text{O}_4$ involving the other half of the tetrahedral sites where Li–Li interactions are absent [35, 36].

A discharge capacity of 95 mAh g^{-1} is obtained at a specific current of 30 mA g^{-1} . Although the theoretical capacity of LiMn_2O_4 corresponding to complete removal and insertion of Li^+ -ions during charge–discharge cycling is 148 mAh g^{-1} , lower values are reported from experimental studies [37–39]. This is because the discharge capacity depends on various properties of the material such as particle size, porosity, morphology, etc., and also on electrochemical experimental conditions. Ahn and Song synthesized LiMn_2O_4 by a solid state reaction in the temperature range from 650 to 900°C and discharge capacity values between 90 and 100 mAh g^{-1} were reported [37]. A discharge capacity of 115 mAh g^{-1} was reported by Lanz

et al. [38], for LiMn_2O_4 prepared by a ceramic process. In another study, Park et al. [39], reported about 115 mAh g^{-1} for a commercial sample of LiMn_2O_4 powder. Thus, the discharge capacity of 95 mAh g^{-1} obtained in the present work for a commercial sample of LiMn_2O_4 is comparable with values reported [37–39].

Impedance spectra of a Li– LiMn_2O_4 coin cell measured at 3.50 V are shown as Nyquist diagrams in Fig. 3, typically, at -10 , 10 , 30 and 50°C . Similar data were obtained at other temperatures. The magnitude of impedance as observed from the size of the Nyquist spectrum decreases with an increase in temperature. A Nyquist plot consists of high frequency intercept on real axis, a broad semicircle in high frequency region and a linear low frequency spike (Fig. 3a–d). The data recorded at -10°C (Fig. 3a) is again presented in Fig. 4 as both Nyquist and Bode plots for the purpose of clarity and analysis. The semicircle in Nyquist diagram (Fig. 4a) is broad and depressed indicating a complex nature of the corresponding resistances and capacitances. The measured impedance is expected to contain contributions from both Li and LiMn_2O_4 electrodes of the coin cell. However, it is known that the kinetics of Li electrode reaction is fast with high exchange current density and the impedance contribution of Li electrode is expected to be low, at least in fresh cells [40, 41]. Li surface develops passivation films in aged cells, and the surface films are likely to retard the kinetics at Li/electrolyte interface and therefore increase its impedance [42]. Because the measurements were made with fresh cells, impedance of Li electrode is considered to be negligibly smaller than the impedance of LiMn_2O_4 electrode. The changes in measured impedance are thus attributed to LiMn_2O_4 electrode. This procedure is similar to what is in practice in the literature [43]. The high frequency intercept on real axis provides ohmic resistance (R_s), which is due to the combined resistances of the electrolyte, separator, current collectors, leads, etc. The depressed semicircle is likely to be due to overlap of two RC time constants. The broad semicircle can be resolved into two semicircles, one semicircle attributed to the combination of resistance (R_f) and capacitance (C_f) of the surface film present on the LiMn_2O_4 electrode; and the other semicircle to the combination of charge-transfer resistance (R_{ct}) of the electron-transfer process and double-layer capacitance (C_{dl}) of the electrode. The low frequency linear spike represents impedance of a diffusion process, which is known as Warburg impedance (W). In an ideal case, the linear data should make a 45° angle to the real axis. In the present study, however, the angle is greater than 45° , probably because of capacitance nature of small particles of LiMn_2O_4 [44], which is ignored in the analysing the impedance data. The simple electrical equivalent circuit, which represents the features of impedance data, is shown

in Fig. 4d. It is known that the impedance of positive electrode materials, for instance, LiCoO_2 is contributed by the surface film resistance [45, 46]. Surface film formation occurs due to the reactivity of the electrode material with the electrolyte. A similar approach in analysis of the impedance of LiMn_2O_4 electrode was adopted in a previous report [32]. A capacitance element is replaced by a constant phase element (CPE), denoted as Q and employed for fitting the experimental data. The use of CPE arises due to distribution of microscopic properties of the electrode material. As the electrode is made of small particles of the electroactive material together with conductive carbon and binder, the interface between the electrode and electrolyte are not uniform. The surface film as well as the electron-transfer process is not uniform throughout the electrode surface. The contributions of resistances and capacitances are different at different regions on the electrode. The semicircles of Nyquist plots are depressed due to these distributions. The impedance representation of CPE is given as [47]:

$$Z = 1/[Q_o(j\omega)^p] \quad (2)$$

where Q_o is an adjustable parameter and $\omega = 2\pi f$, f being frequency of the ac signal. For $p = 0$, CPE represents a resistance, $R (=Q_o^{-1})$; for $p = 1$, a capacitance, $C (=Q_o)$; for $p = 0.5$, a Warburg impedance; and for $p = -1$, an inductance, $L (=Q_o^{-1})$. The impedance spectrum (Fig. 4) was subjected to NLLS procedure using the electrical equivalent circuit (Fig. 4d). Assignment of an exact equivalent circuit is quite difficult. Jamnik and Maier [48–50] derived an equivalent circuit which took account of electrical and chemical parameters for cells with a mixed conductor of electronic and ionic charges. These transmission-line models are quite complex and difficult to analyze experimental results. Furthermore, the effect of particle size distribution on insertion processes is a study of theoretical interest [31]. In the present study, the particle size of LiMn_2O_4 is broadly distributed. Hence the circuit shown in Fig 4d is simple and convenient for analysis of the experimental data. Finite length Warburg [47] was employed and the corresponding parameters, namely, W_s -R, W_s -T and W_s -P, were obtained from the fit results. Approximate initial values of the parameters were assigned and the best fit parameters were displayed after several iterations. In Fig. 4a–c, the experimental data are shown as open circles and the theoretical impedance spectrum simulated from the fit results is shown as a smooth curve. The theoretical spectrum agrees well with the experimental spectrum. Furthermore, χ^2 parameter (which is a judging parameter for goodness of a least squares fit) of fitting is 1×10^{-4} . These results suggest that the fitting procedure is fairly reliable. The fit results are shown in Table 1. The above procedure was adopted for all impedance spectra

measured at 3.50 V. The impedance spectra recorded at 3.60, 3.70 and 3.80 V and in the temperature range -10 to 50 °C were similar to the spectra recorded at 3.50 V with two semicircles. However, the 3.90 V data consist of three semicircles in the temperature range -10 to 20 °C, as described below.

Impedance spectra recorded at 3.90 V are shown as Nyquist plots in Fig. 5, typically, at four temperatures (-10 , 10 , 30 and 50 °C). At -10 °C, the plot (Fig. 5a) consists of three semicircles instead of two semicircles observed at 3.50 V and -10 °C (Fig. 3a). Similar three semicircle Nyquist diagrams were also recorded at -5 , 0 , 5 and 10 °C at 3.90 V. However, the Nyquist plot at 30 °C (Fig. 5c) consists of only two semicircles, similar to the data recorded at 3.50 V at all temperatures (Fig. 3). The spectra recorded between 15 and 50 °C are alike. These findings are consistent with the results reported by Zhuang et al. [32]. The high frequency semicircle was related to the Li^+ ion migration through the surface film covered on the spinel LiMn_2O_4 , the middle frequency semicircle was attributed to charge-transfer through the electrode/electrolyte interface and the low frequency linear spike was assigned to solid state diffusion of the Li^+ ion in the LiMn_2O_4 matrix [32, 51–53]. The additional semicircle appearing at middle to high frequency range (MHFS) is

attributed to electronic property of the material on the basis of the influence of temperature on its appearance, similar to the results obtained in the present study. Furthermore, the conclusions of Zhuang et al. [32] were supported by the suggestion of Nobili et al. [54] that the effect of electronic conductivity of the material should be reflected in the Nyquist diagrams. On the basis of atom model, the intercalation–deintercalation process was described to follow adsorption of desolvated Li^+ ions on the electrode surface [54]. The process was contributed to accompany the insertion of electrons into the conduction band of the electrode material with simultaneous diffusion of Li^+ ions from the electrolyte for incorporation into the crystal lattice. On the basis of studies on Li_xCoO_2 , metallic conductivity of the material was considered only when x reaches 0.95 and electron flow was limited by low conductivity of the material [54]. Electronic conduction and Li^+ ion lattice incorporation were considered as rate-limiting steps of the overall charge-transfer process for $x > 0.95$ and $x < 0.95$, respectively. A similar approach was adopted by Zhuang et al. [32] for LiMn_2O_4 . The electronic resistance dominates at low intercalation stages (high potentials) and low temperatures in the present studies also as described above.

The MHFS semicircle is clearly visible at low temperature (-10 °C) and the diameter of the semicircle

Fig. 3 Impedance spectra of $\text{Li}/\text{LiMn}_2\text{O}_4$ cell at 3.50 V at **a** -10 , **b** 10 , **c** 30 and **d** 50 °C. Frequency values in Hz are indicated for a few data points. Area: 2.0 cm^2 and mass of LiMn_2O_4 : 5.0 mg cm^{-2}

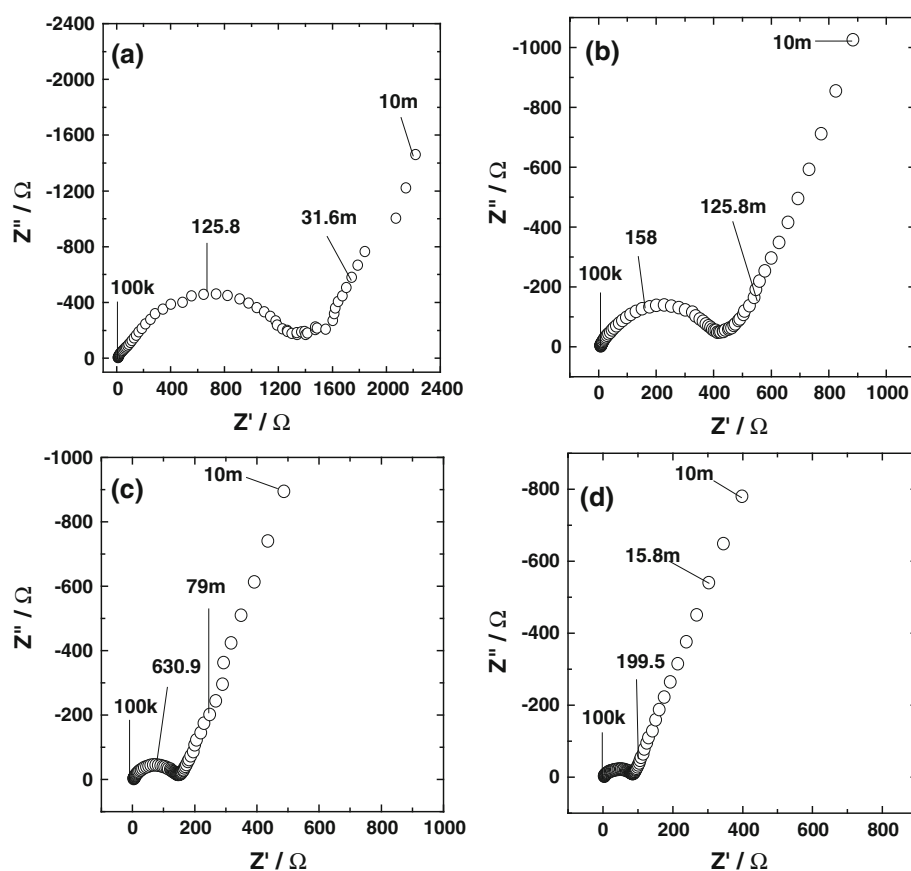


Fig. 4 Impedance spectra of Li/LiMn₂O₄ cell at 3.50 V and -10°C in **a** Nyquist, **b** Bode phase, **c** Bode phase angle representations and **d** electric equivalent circuit. Frequency values in Hz are indicated for a few data points in **a**. Area: 2.0 cm^2 and mass of LiMn₂O₄: 5.0 mg cm^{-2}

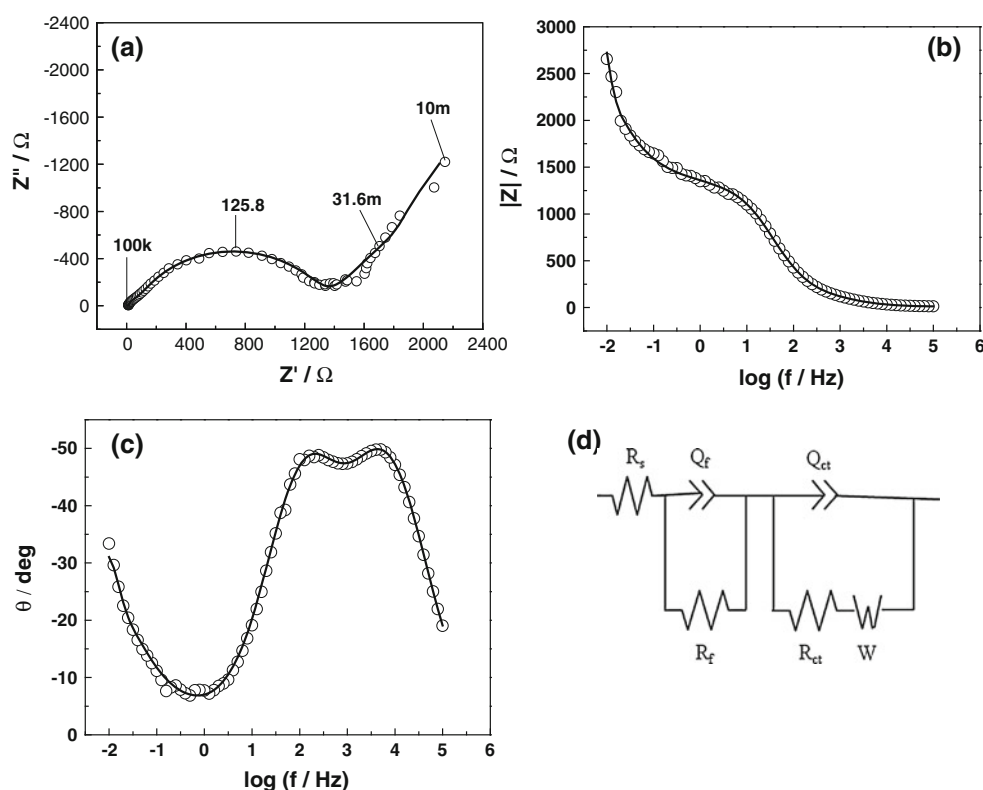


Table 1 Fit results of EIS at 3.50 V and -10°C

Parameter	Value	Error (%)
R_s	$21.24\ \Omega$	0.38
R_f	$145.52\ \Omega$	0.52
$Q_{o(f)}$	$9.56 \times 10^{-6}\ \text{F s}^{p-1}$	1.69
P_f	0.79	0.21
R_{ct}	$2,506\ \Omega$	10.13
$Q_{o(ct)}$	$1.35 \times 10^{-5}\ \text{F s}^{p-1}$	10.8
P_{ct}	0.80	0.39
$W_s\text{-}R$	$3,138\ \Omega$	8.83
$W_s\text{-}T$	$57.3\ \text{s}$	17.1
$W_s\text{-}P$	0.58	2.86

decreases with an increase in temperature indicating a decrease in the value of the electronic resistance of LiMn₂O₄ at high temperatures. Thus, the impedance spectra recorded at 3.90 V at different temperatures fall into two categories: Nyquist plots consisting of three semicircles at temperature $\leq 10^{\circ}\text{C}$ and those consisting of two semicircles at temperature $\geq 15^{\circ}\text{C}$. The data recorded at -10°C are again shown in Fig. 6 as both Nyquist and Bode forms for the purpose of analysis. The electrical equivalent circuit, which was found to fit the experimental data, is shown in Fig. 6d. In addition to the impedance parameters shown in Fig. 4d, electronic resistance (R_e) and the corresponding CPE (Q_e) are included in Fig. 6d. Nobili

et al. [43] employed an equivalent circuit consisting of R_e and Q_e for analysis of impedance of LiCoO₂ electrodes. The element Q_e takes account of rough nature of the electrode and random orientation of crystallites inside active material grains [43]. The equivalent circuits presented in Fig. 6d deviates from the circuit used by Zhuang et al. [32] in the position of Warburg element. The Warburg element (W) is placed in series with R_{ct} , which in turn are in parallel to the CPE corresponding to double-layer capacitance (Fig. 6d). This is in consistence with the Randles equivalent circuit [55]. The spectrum was subjected to NLLS fitting, and impedance parameters were evaluated. The theoretical impedance curves generated from the fit results agree well with the experimental data (Fig. 6). The χ^2 fitting parameter is about 1×10^{-4} , and the errors are generally less than 10 %. The fit results of EIS recorded at 3.90 V and -10°C are shown in Table 2. It was seen that there was a good agreement between the experimental data and simulated spectra for the data recorded between -10 and 10°C . The data measured at temperature $\geq 15^{\circ}\text{C}$ were analysed using equivalent circuit presented in Fig. 4d. The impedance spectra recorded in the potential range 4.00–4.30 V resemble the data measured at 3.90 V in consisting of three semicircles at low temperatures and two semicircles at high temperature range.

The above procedures were employed for analysis of all impedance data and the variations of different resistances

Fig. 5 Impedance spectra of Li/LiMn₂O₄ cell at 3.90 V at **a** –10, **b** 10, **c** 30 and **d** 50 °C. Frequency values in Hz are indicated for a few data points. Area: 2.0 cm² and mass of LiMn₂O₄: 5.0 mg cm^{–2}

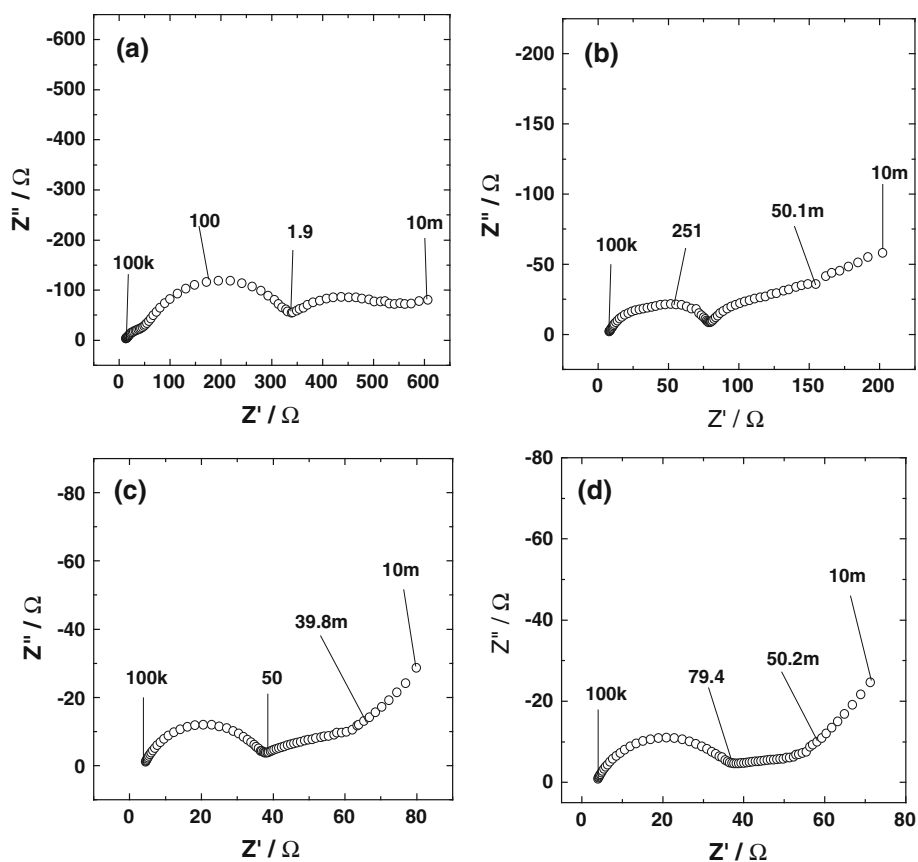


Fig. 6 Impedance spectra of Li/LiMn₂O₄ cell at 3.90 V and –10 °C in **a** Nyquist, **b** Bode phase, **c** Bode phase angle representations and **d** electric equivalent circuit. Frequency values in Hz are indicated for a few data points in **a**. Area: 2.0 cm² and mass of LiMn₂O₄: 5.0 mg cm^{–2}

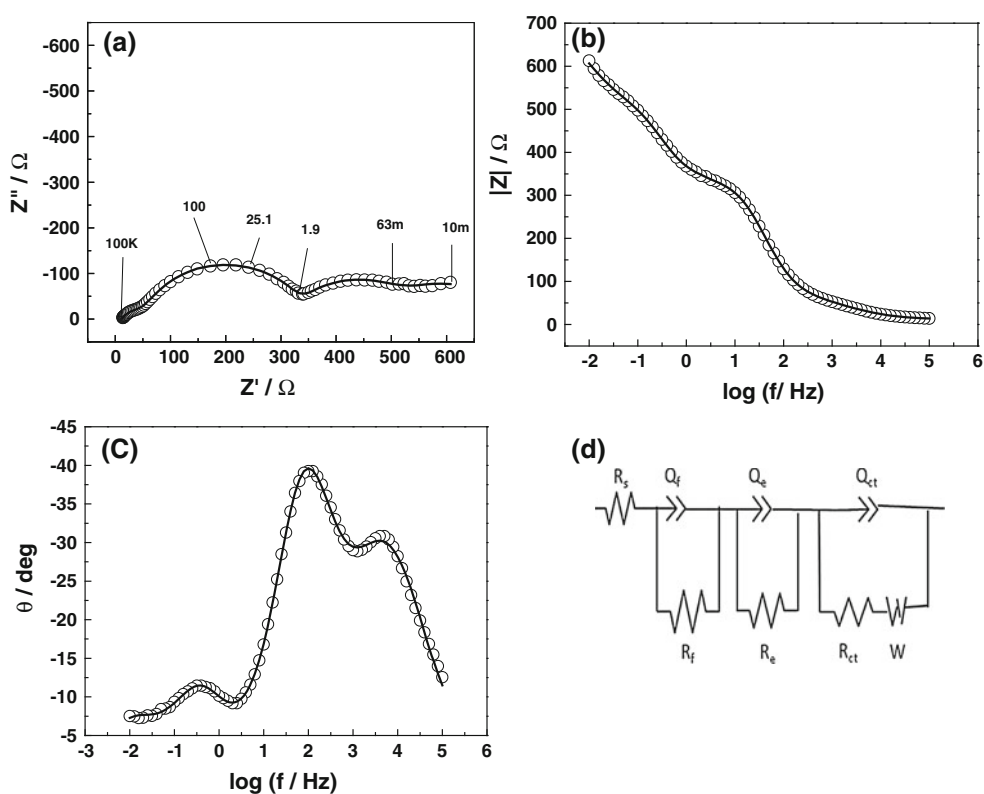


Table 2 Fit results of EIS at 3.90 V and -10°C

Parameter	Value	Error (%)
R_s	$24.4\ \Omega$	0.54
R_f	$95.42\ \Omega$	1.85
$Q_{o(f)}$	$3.22 \times 10^{-5}\ \text{F s}^{p-1}$	5.06
P_f	0.69	0.71
R_e	$289.4\ \Omega$	3.29
$Q_{o(e)}$	$4.73 \times 10^{-3}\ \text{F s}^{p-1}$	0.52
P_e	0.86	4.2
R_{ct}	$524.4\ \Omega$	10.95
$Q_{o(ct)}$	$3.28 \times 10^{-5}\ \text{F s}^{p-1}$	3.49
P_{ct}	0.89	0.62
$W_s\text{-}R$	$4,433\ \Omega$	19.76
$W_s\text{-}T$	$5.46\ \text{s}$	34.94
$W_s\text{-}P$	0.47	11.75

with potential and temperatures were examined. The variation of R_s ($\Omega\ \text{cm}^2$) with potential at various temperatures is plotted in Fig. 7a. R_s are nearly invariant with potential at a particular temperature while a large change is observed on changing the temperature. The R_s decreases with an increase in temperature at a given potential. For instance at 3.50 V, the value of R_s is $21.0\ \Omega\ \text{cm}^2$ at -10°C and it decreases to $6.0\ \Omega\ \text{cm}^2$ at 50°C . It is noticed that $(1/R_s)$ follows Arrhenius behaviour (Fig. 7b). Apparent values of energy of activation calculated from slope of linear plot in Fig. 7b for conduction process of R_s are 0.16, 0.14 and $0.14\ \text{eV}$, respectively, at 3.50, 3.90 and $4.20\ \text{V}$. As the major contribution for R_s is from the electrolyte resistance, the apparent activation energy is likely to be that of electrolyte conduction process.

The variations of R_e (in $\Omega\ \text{cm}^2$) with voltage (3.90–4.20 V) in the temperature range from -10 to 10°C are shown in Fig. 8a. There is a decrease in R_e with an increase in voltage from 3.90 to $4.20\ \text{V}$ at a given temperature. This is similar to the observations made at 10°C by Zhuang et al. [32] Also, the value of R_e decreases indicating an increase in the electronic conductivity of LiMn_2O_4 with an increase in temperature from -10 to 10°C . Plots of $\log(1/R_e)$ versus $(1/T)$ are presented in Fig. 8b. It is seen that the data follow Arrhenius behaviour. The values of energy of activation calculated are 0.71, 0.69, 0.62 and $0.65\ \text{eV}$, respectively, at 3.90, 4.00, 4.10 and $4.20\ \text{V}$.

The R_{ct} (in $\Omega\ \text{cm}^2$) values are plotted against voltage in the temperature range of -10 to 50°C and shown in Fig. 9a. There is a decrease in R_{ct} with an increase in potential up to $4.10\ \text{V}$, and thereafter there is a slight increase in the potential range from 4.10 to $4.30\ \text{V}$. The decrease in R_{ct} between 3.50 and $4.10\ \text{V}$ is quite significant at low temperature (-10 to 15°C). At -10°C for

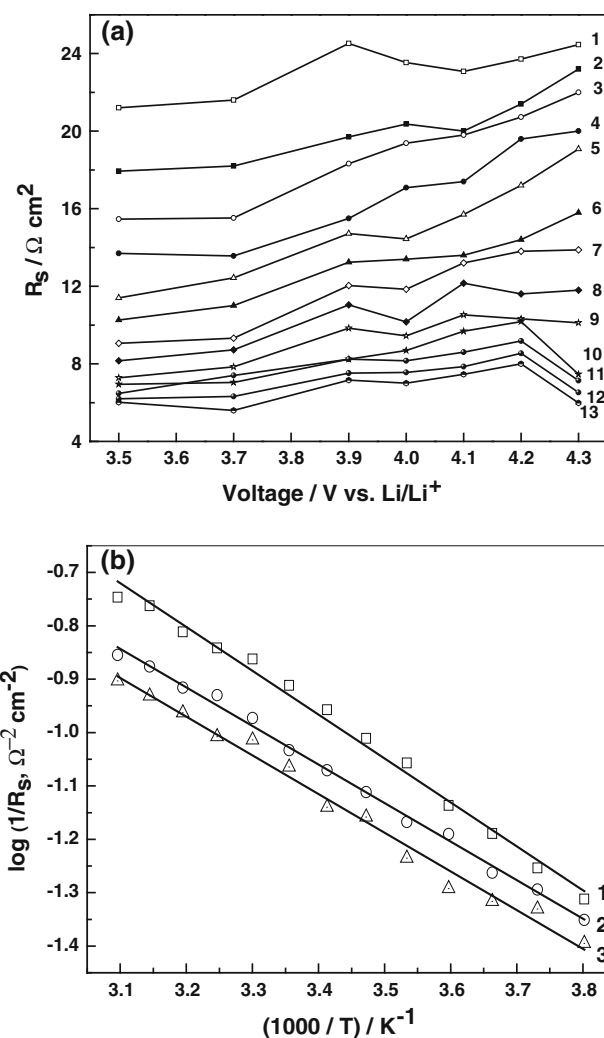


Fig. 7 **a** Ohmic resistance (R_s) versus cell voltage at different temperature: 1 -10 , 2 -5 , 3 0, 4 5, 5 10, 6 15, 7 20, 8 25, 9 30, 10 35, 11 40, 12 45 and 13 50°C . **b** Plots of $\log(1/R_s)$ versus $(1,000/T)$ at different cell voltages: 1 3.50, 2 3.90 and 3 $4.20\ \text{V}$. Area: $2.0\ \text{cm}^2$ and mass of LiMn_2O_4 : $5.0\ \text{mg cm}^{-2}$

instance, R_{ct} is $2,500\ \Omega\ \text{cm}^2$ at $3.50\ \text{V}$ and decrease to about $200\ \Omega\ \text{cm}^2$ at $4.10\ \text{V}$. But at 30°C , the value of R_{ct} is $300\ \Omega\ \text{cm}^2$ and it decreases to about $100\ \Omega\ \text{cm}^2$ at $4.10\ \text{V}$. These results indicate that the kinetics of electron-transfer process in LiMn_2O_4 is markedly slow at low temperatures when the oxide is close to the fully intercalated stage. The appearance of a minimum in R_{ct} at $4.10\ \text{V}$ is similar to the variation of R_{ct} with potential at 10°C [32]. This also agrees with the report that R_{ct} exhibits a minimum in the voltage region where capacity peaks are present in the plot of differential capacity versus potential [56]. The temperature dependence of R_{ct} is very high at low potentials and it is low at high potentials (Fig. 9a).

The charge-transfer reaction at LiMn_2O_4 electrode involves a change in the oxidation state of Mn and

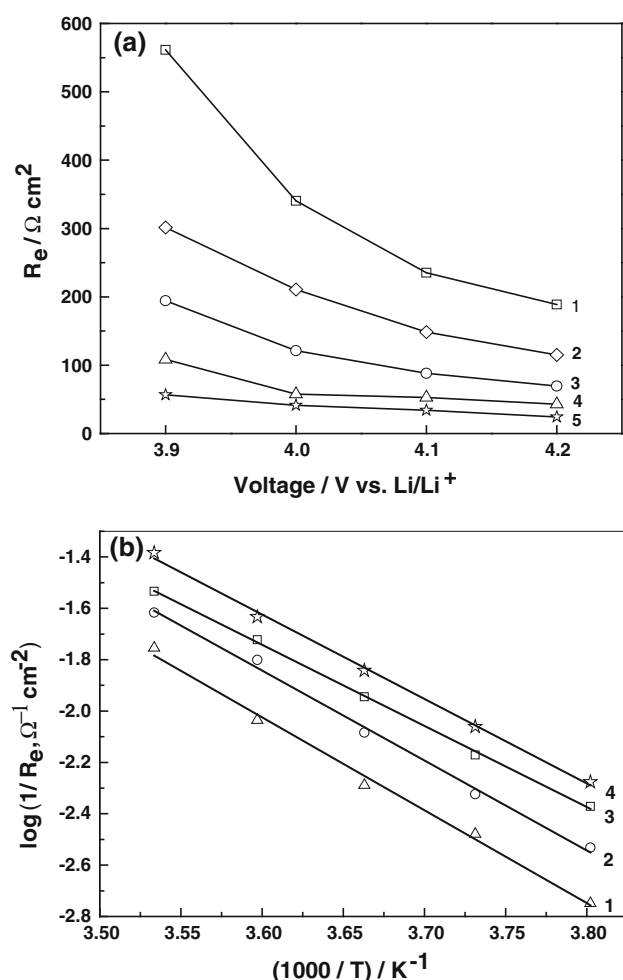


Fig. 8 **a** Electronic resistance (R_e) versus cell voltage at different temperature: 1 –10, 2 –5, 3 0, 4 5 and 5 10 °C. **b** Plot of $\log(1/R_e)$ versus $(1,000/T)$ at different cell voltages: 1 3.90, 2 4.00, 3 4.10 and 4 4.20 V. Area: 2.0 cm^2 and mass of LiMn_2O_4 : 5.0 mg cm^{-2}

insertion/de-insertion of Li^+ ion into/from the tunnel structure of the compound (Reaction 1). R_{ct} obtained from the analysis of impedance spectra is related to exchange current density of $\text{Mn}^{3+}/\text{Mn}^{4+}$ redox process by Eq. (3).

$$R_{ct} = RT/(F I_0) \quad (3)$$

where I_0 is exchange current density (in A cm^{-2}) and the other symbols have their usual meanings. The values of I_0 were calculated and the variation of I_0 with potential at several temperatures is shown in Fig. 9b. It is seen that I_0 increases with T and also with potential (Fig. 9b). It was shown that $(R_{ct} T^{-1})$ is related to activation energy of the electron-transfer process [17]. Plot of $\log(1/R_{ct} T^{-1})$ versus $(1/T)$ are shown in Fig. 10. The values of activation energy calculated are 0.37, 0.30 and 0.42 eV, respectively, at 3.50, 3.90 and 4.10 eV.

The chemical diffusion coefficient of Li^+ ions (D_{Li}) into LiMn_2O_4 was evaluated from the impedance spectroscopy.

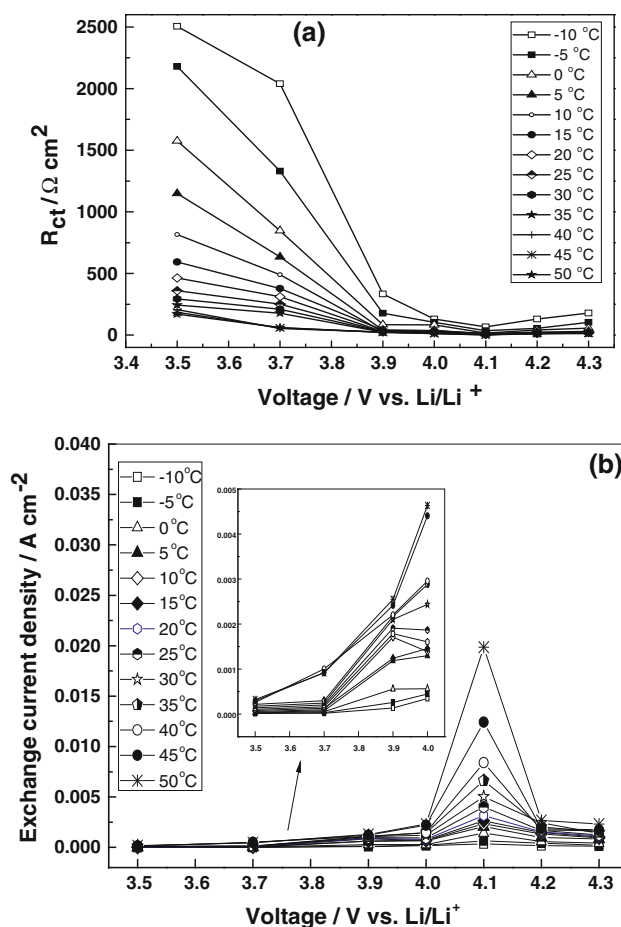


Fig. 9 **a** Variation of R_{ct} with cell voltage at different temperature and **b** exchange current density (I_0) with cell voltage at different temperatures. Area: 2.0 cm^2 and mass of LiMn_2O_4 : 5.0 mg cm^{-2}

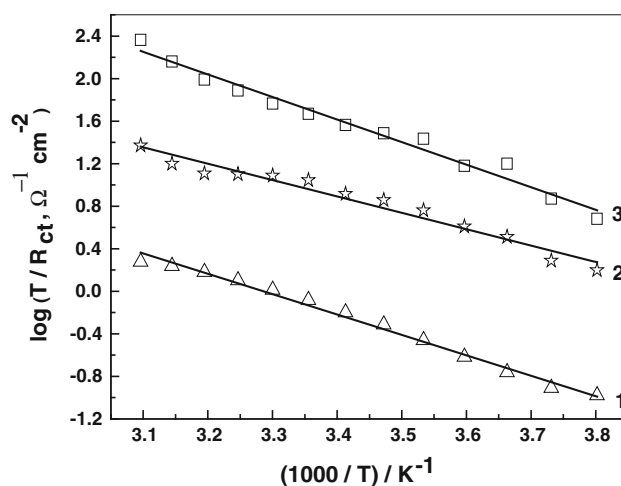


Fig. 10 Plot of (T/R_{ct}) versus $(1/T)$ at different voltages: 1 3.50, 2 3.90 and 3 4.10 V. Area: 2.0 cm^2 and mass of LiMn_2O_4 : 5.0 mg cm^{-2}

The real (Z') component of impedance (Z) in the low frequency linear regime can be expressed by the following equation [57]:

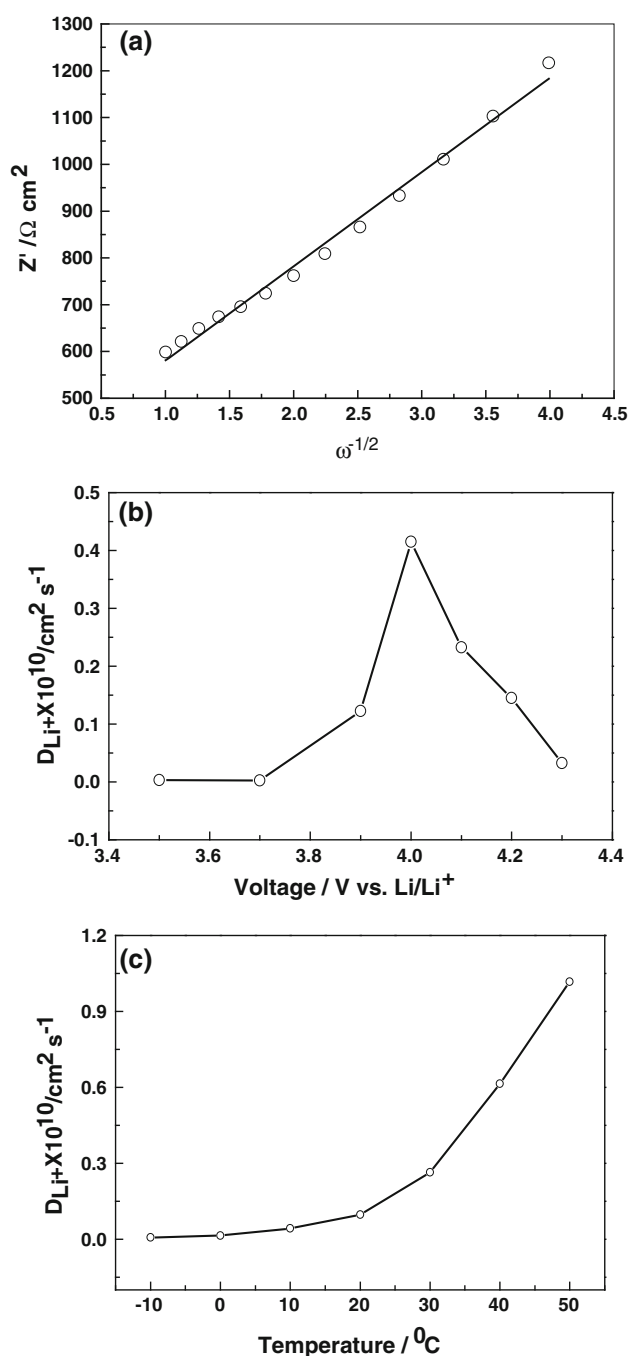


Fig. 11 **a** Plot of real part (Z') versus $\omega^{-1/2}$, **b** variation of diffusion coefficient with cell voltage at 20 °C and **c** variation of diffusion coefficient with temperature at 3.90 V. Area: 2.0 cm^2 and mass of LiMn_2O_4 : 5.0 mg cm^{-2}

$$Z' = R_T + \sigma \omega^{-1/2} \quad (4)$$

where σ is Warburg factor and R_T is total resistance ($=R_s + R_{ct} + R_e$). A plot of Z' versus $\omega^{-1/2}$ from impedance data measured at 20 °C and 3.90 V is shown in Fig. 11a. The slope of the plot provides the value of σ

(27.2 $\Omega \text{ cm}^2 \text{ s}^{-1/2}$). The value of D_{Li} is calculated from the following equation [58]:

$$D_{Li} = R^2 T^2 / 2 A^2 F^4 c^2 \sigma^2 \quad (5)$$

where R is the gas constant, T is the temperature, A is the area of electrode (2.0 cm^2), F is Faraday's constant (96,500 C), c is concentration of Li-ion ($1 \times 10^{-3} \text{ mol cm}^{-3}$). The value of D_{Li} obtained for the data shown in Fig. 11a is $1 \times 10^{-11} \text{ cm}^2 \text{ s}^{-1}$. The variation in D_{Li} with voltage at 20 °C is shown in Fig. 11b. The values of D_{Li} are found to be in the range of 2.5×10^{-12} – $4.1 \times 10^{-11} \text{ cm}^2 \text{ s}^{-1}$. These values of D_{Li} are in close agreement with the reported values [59]. There is an increase in the value of D_{Li} with increase in the voltage from 3.50 to 4.00 V and a maximum value of D_{Li} ($4.1 \times 10^{-11} \text{ cm}^2 \text{ s}^{-1}$) is obtained at 4.00 V, the voltage corresponding to the first plateau in the charging process of LiMn_2O_4 . After this, there is a gradual decrease in the value of D_{Li} in the voltage range of 4.00–4.30 V. The values of D_{Li} are also evaluated at various temperatures in the range of -10 to 50 °C at the voltage of 3.90 V and are shown in Fig. 11c. The value of D_{Li} is found to increase with an increase in temperature. The values of D_{Li} are in the range from 8.3×10^{-13} to $1.0 \times 10^{-10} \text{ cm}^2 \text{ s}^{-1}$.

4 Conclusions

Ac impedance of LiMn_2O_4 electrodes were measured at several temperatures and potentials. The Nyquist plots consisted of semicircles corresponding to two RC time constants at high temperatures and low potentials. However, at low temperature range (-10 to 10 °C) and potential region between 3.90 and 4.20 V, three time constants appeared. The third semicircle present at MHFS was due to electronic resistance of LiMn_2O_4 , which showed up clearly at partial delithiation stages. Impedance parameters were evaluated using appropriate electrical equivalent circuits. From the temperature dependence of resistive parameters, activation energy values for the corresponding processes were calculated.

Acknowledgement Financial support from India Science Lab, General Motors Global R&D, is gratefully acknowledged.

References

- Kim TH, Park JS, Chang SK, Choi S, Ryu JH, Song H-K (2012) *Adv Energy Mater* 2:860–872
- Terada N, Yanagi T, Arai S, Yoshikawa M, Ohta K, Nakajima N, Yanai A Arai (2001) *J Power Sources* 100:80–92
- Dunn B, Kamath H, Tarascon JM (2011) *Science* 334:928–938

4. Thackeray MM, David WIF, Bruce PG, Goodenough (1983) *Mater Res Bull* 18:461–472
5. Cho J, Thackeray MM (1999) *J Electrochem Soc* 146:3577–3581
6. Tarascon JM, Guyomard D (1994) *Solid State Ion* 69:222–237
7. Tarascon JM, Mackinnon WR, Coowar F, Bowmer TN, Amatucci G, Guyomard D (1991) *J Electrochem Soc* 141:1421–1431
8. Tarascon JM, Wang E, Shokoohi FK, Mckinnon WR, Coloson S (1991) *J Electrochem Soc* 138:2859–2864
9. Macdonald JR (1987) *Impedance spectroscopy*. Wiley, New York
10. Park SM, Yoo JS (2003) *Anal Chem* 75:455A–461A
11. Rodrigues S, Munichandraiah N, Shukla AK (2000) *J Power Sources* 87:12–20
12. Huet FJ (1998) *J Power Sources* 70:59–69
13. Hampson NA, Karunathilaka SAGR, Leck R (1980) *J Appl Electrochem* 10:3–11
14. Sathyanarayana S, Venugopalan S, Gopikanth ML (1979) *J Appl Electrochem* 9:125–139
15. Suresh P, Nagaraju DH, Shukla AK, Munichandraiah N (2005) *Electrochim Acta* 50:3262–3272
16. Rodrigues S, Munichandraiah N, Shukla AK (1999) *J Solid State Electrochem* 3:397–405
17. Suresh P, Shukla AK, Munichandraiah N (2002) *J Appl Electrochem* 32:267–273
18. Dunn RP, Kable J, Krause FC, Hwang C, Ratnakumar BV, Smart MC, Lucht BL (2012) *J Electrochem Soc* 159:A2100–A2108
19. Nam ND, Park IJ, Kim JG, Kim HS (2012) *Mater Res Bull* 47:2811–2814
20. Qin Y, Chen Z, Lu W, Amine K (2010) *J Power Sources* 195:6888–6892
21. Shim EG, Nam TH, Kim JG, Kim HS, Moon SI (2008) *J Power Sources* 175:533–539
22. Rui XH, Jin Y, Feng XY, Zhang LC, Chen CH (2011) *J Power Sources* 196:2109–2114
23. Zhang Y, Wang CY (2009) *J Electrochem Soc* 156:A527–A535
24. Kang SH, Abraham DP (2007) *J Power Sources* 174:1229–1233
25. Suresh P, Shukla AK, Munichandraiah N (2006) *J Power Sources* 161:1307–1313
26. Suresh P, Rodrigues SR, Shukla AK, Vasan HN, Munichandraiah (2005) *Solid State Ion* 176:281–290
27. Andre D, Meiler M, Steiner K, Walz H, Soczka-Guth T, Sauer DU (2011) *J Power Sources* 196:5349–5356
28. Kulova TL, Tarnopolskii VA, Skindin AM (2009) *Russ J Electrochem* 45:38–44
29. Ratnakumar BV, Smart MC, Whitcanack LD, Ewell RC (2006) *J Power Sources* 159:1428–1439
30. Srinivasan R, Carkhuff BG, Butler MC, Baisden AC (2011) *Electrochim Acta* 56:6198–6204
31. Bruce PG, Saidi MY (1992) *J Electroanal Chem* 322:93–105
32. Zhuang QC, Wei T, Du LL, Cui YL, Fang L, Sun SG (2010) *J Phys Chem C* 114:8614–8621
33. Nupur NN, Munichandraiah N (2008) *J Solid State Electrochem* 12:1619–1627
34. Zhuang QC, Fan XY, Xu JM, Wei GZ, Dong QF, Sun SG (2008) *Chem Res Chin Univ* 24:511–515
35. Xia Y, Yoshio (1996) *J Electrochem Soc* 143:825–833
36. Hwang BJ, Santhanam R, Liu DG (2001) *J Power Sources* 97/98:443–446
37. Ahn DS, Song MY (2000) *J Electrochem Soc* 147:874–879
38. Lanz M, Kormann C, Steninger H, Heil G, Hass O, Novak P (2000) *J Electrochem Soc* 147:3997–4000
39. Park SC, Kim YM, Kang YM, Kim KT, Lee PS, Lee J (2001) *J Power Sources* 103:86–92
40. Munichandraiah N, Scanlon LG, Marsh RA, Kumar B, Sircar AK (1994) *J Electroanal Chem* 379:495–499
41. Zaban A, Aurbach D (1995) *J Power Sources* 54:289–295
42. Goverscek M, Jamnik J, Pejovnik S (1993) *J Electrochem Soc* 140:308–314
43. Nobili F, Dsoke S, Minicucci M, Croce F, Marassi R (2006) *J Phys Chem B* 110:11310–11313
44. Diard JP, Le Gorrec B, Montella C (2001) *J Electroanal Chem* 499:67–77
45. Thomas MGSR, Bruce PG, Goodenough JB (1985) *J Electrochem Soc* 132:1521–1528
46. Aurbach D, Levi MD, Levi E, Schechter A (1997) In: Abstracts of joint international meeting on batteries and fuel cells for portable applications and electric vehicles, The Electrochemical Society, Pennington, NJ, p 124
47. ZPlot for Windows, (2001) *Electrochemical Impedance Software Operating manual*, Scribner Associates, Inc., USA p. 8.1
48. Jamnik J, Maier J (2001) *Phys Chem Chem Phys* 3:1668–1678
49. Jamnik J, Maier J (1999) *J Electrochem Soc* 146:4183–4188
50. Jamnik J (2003) *Solid State Ion* 157:19–28
51. Aurbach D, Levi MD, Levi E, Telier H, Markovsky B, Salitra G, Heider U, Hekier L (1998) *J Electrochem Soc* 145:3024–3034
52. Aurbach D, Gamolsky K, Markovsky B, Salita G, Gofer Y, Heider U, Hekier L (2000) *J Electrochem Soc* 147:1322–1331
53. Aurbach D, Levi MD, Gamulski K, Markovsky B, Salitra G, Levi E, Heider U, Heider L, Oester R (1999) *J Power Sources* 81–82:472–479
54. Nobili F, Tossici R, Crose F, Scrosati B, Marassi R (2001) *J Power Sources* 94:238–241
55. Greef R, Peat R, Peter LM, Pletcher LM, Robinson (1985) *Instrumental methods in electrochemistry*. Wiley, New York 251
56. Zhang SS, Xu K, Jow TR (2004) *Electrochim Acta* 49:1057–1061
57. Ji SZ, Zhang JY, Wang WW, Huang Y, Feng ZR, Zhang ZT, Tang ZL (2010) *Mater Chem Phys* 123:510–515
58. Bard AJ, Faulkner LR (2004) *Electrochemical methods: fundamentals and applications*, 2nd edn. Wiley, New Delhi, p 368
59. Kim SW, Pyun SI (2002) *J Electroanal Chem* 528:114–120